www.acsmaterialsletters.org

An Exfoliation—Evaporation Strategy To Regulate N Coordination Number of Co Single-Atom Catalysts for High-Performance Lithium—Sulfur Batteries

Daliang Fang, Pan Sun, Shaozhuan Huang, Yang Shang, Xueliang Li, Dong Yan, Yew Von Lim, Ching-Yuan Su, Bing-Jian Su, Jenh-Yih Juang, and Hui Ying Yang*



Downloaded via ARGONNE NATL LABORATORY on January 14, 2022 at 17:12:07 (UTC). See https://pubs.acs.org/sharingguidelines for options on how to legitimately share published articles.

Cite This: ACS Materials Lett. 2022, 4, 1-10



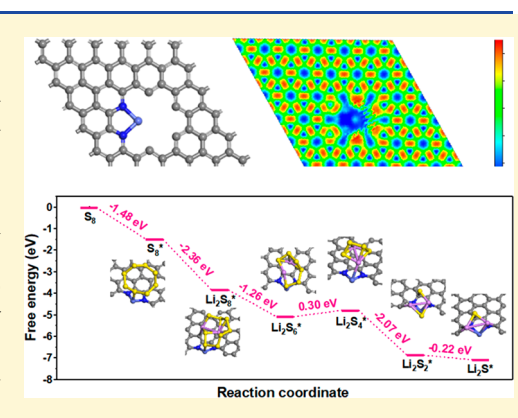
ACCESS

Metrics & More

Article Recommendations

Supporting Information

ABSTRACT: Single-atom catalysts (SACs) with metal-nitrogen (M-N) moiety are effective in boosting the redox kinetics of lithium-sulfur (Li-S) batteries. However, the precise preparation of SACs with controllable M-N coordination number remains challenging and the relationship between M-N coordination number and polysulfide redox kinetics is still unexplored. Herein, a novel exfoliation-evaporation strategy assisted by molten salt is proposed to fabricate Co SACs (named Co-N_x) with different N coordination numbers for Li-S batteries. The key of this strategy is to exfoliate layered Cobased ZIF-L precursors into N-doped graphene with abundant dispersed Co atoms by molten salt and then control Co-N coordination number by selectively introducing Zn evaporation to promote C-N fragments release. Experimental and theoretical calculation results reveal that highly unsaturated Co-N₂ with asymmetric electron distribution immobilizes LiPSs, accelerates LiPSs conversion, and promotes Li₂S deposition/dissociation more effectively



than Co-N₄ through stronger chemical interactions. As a result, Co-N₂ endows Li-S batteries with long cycle life (0.05% capacity decay per cycle for 700 cycles), excellent rate capability (687 mAh g⁻¹ at 5 C), and high areal capacity of 8.2 mAh cm⁻² at a high loading of 7.0 mg cm⁻². This work provides an effective strategy to fabricate SACs with controllable N coordination number and establishes the relationship between M-N coordination number and LiPSs redox kinetics, motivating future rational design of SACs for high-performance Li-S batteries.

INTRODUCTION

Lithium-sulfur (Li-S) battery is a promising next-generation energy storage device, because of its outstanding theoretical capacity (1675 mAh g⁻¹) and energy density (2600 Wh k g⁻¹).^{1,2} However, the shuttle effect of polysulfides (LiPSs) and sluggish reaction kinetics of sulfur species seriously impede its practical application as a favorable postlithium technology.³⁻⁷ Recently, various metal compounds (e.g., TiO₂, ⁸ VS₄, ⁹ CoSe₂, ¹⁰ TiN, ¹¹ CoP¹²) have been employed to immobilize LiPSs and catalyze their conversion to solve the problems. Unfortunately, the following issues persist: (1) The electrical conductivities of these metal compounds are still unsatisfied. (2) Their high densities and mass loadings would compromise the overall energy densities of Li-S batteries. (3) The exposed active sites are still limited, although these metal compounds are nanomaterials. Therefore, it is highly desired to explore lightweight alternative catalysts with outstanding electrical

conductivity and abundant catalytic active sites to realize the practical application of Li-S batteries in the future.

Single-atom catalysts (SACs) usually possess excellent electrical conductivities and can achieve high electrocatalytic activities with almost 100% atomic utilizations. 13-15 SACs have attracted much attention in Li-S batteries, since they can efficiently enhance the chemical interaction with LiPSs and expedite LiPSs redox kinetics through Lewis acid-base interaction with very low mass loadings. 16-19 Generally, the active sites of the common SACs are the $M-N_4$ moiety (M =

Received: July 16, 2021 Accepted: September 23, 2021 Published: November 24, 2021





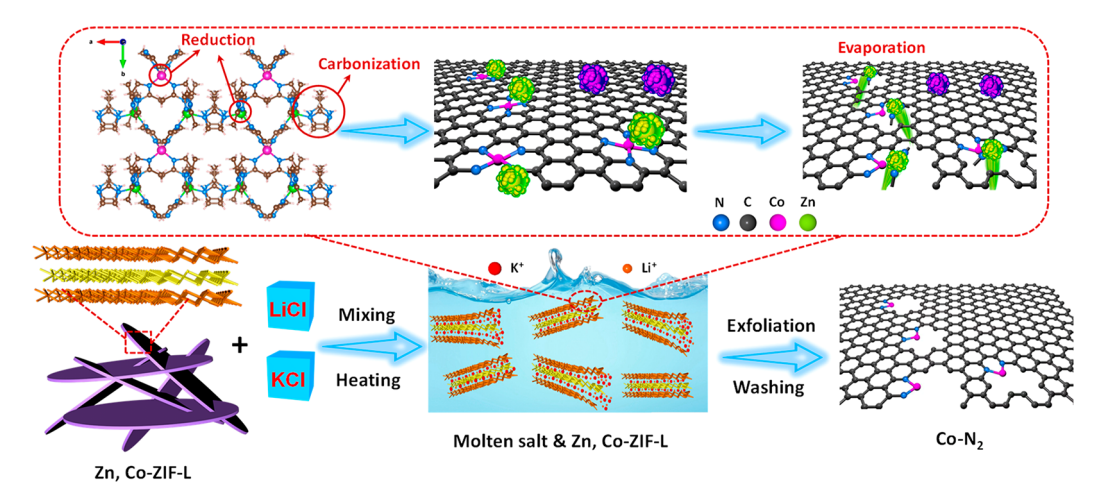


Figure 1. Schematic illustration of Co-N₂ composite synthesis.

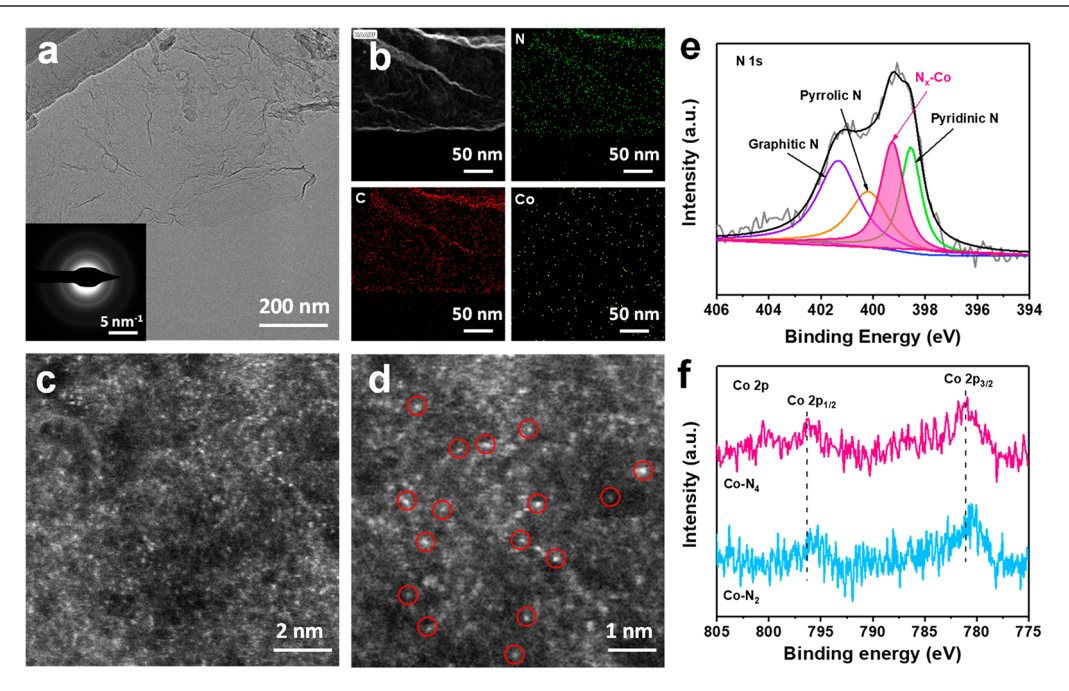


Figure 2. Morphology and composition analysis of $Co-N_2$ composite. (a) TEM image (the inset image is corresponding SAED pattern). (b) EDS mapping of Co, C, and N elements. (c, d) High-resolution HAADF-STEM images. (e) High-resolution XPS N 1s spectrum. (f) High-resolution XPS Co 2p spectra of $Co-N_4$ and $Co-N_2$.

Co,²⁰ Ni,²¹ Fe,²² etc.). However, the symmetric electron distribution in the M-N₄ moiety is not conductive to the adsorption and activation of reaction intermediates, leading to limited electrochemical performance.²³ Compared with M-N₄, highly unsaturated M-N₂ coordination structure possesses increased unoccupied 3d orbitals of metal atom centers, which can promote active material adsorption and interfacial charge transfer.^{24,25} It can be expected that more unoccupied 3d orbitals in metal centers also benefit the Lewis acid-base interaction with S_n²⁻ (typical electron donor) of LiPSs, rendering SACs with M-N₂ sites a highly promising electrocatalyst for Li-S batteries. Recently, two works have demonstrated that M-N2 can facilitate electrocatalytic conversion of LiPSs to improve the electrochemical properties of Li–S batteries obviously. ^{26,27} Will M–N₂ be superior to M– N₄ for accelerating LiPSs redox kinetics? As far as we know, there is no report that has addressed the question. However, the answers to the question are interesting and important for

deeply understanding the atomic structure—activity mechanism of SACs on catalyzing LiPSs conversion, which can provide theoretical direction for future design of advanced SACs applied into Li–S batteries. In addition, it is still quite difficult to realize precise control over the N coordination number of SACs, ^{26,28} which must explore more novel strategies.

Herein, we proposed an exfoliation-evaporation strategy assisted by molten salt to fabricate Co SACs (named $Co-N_x$) with different N coordination numbers by introducing molten salt into the pyrolysis of Co-based ZIF-L precursors, where molten salt exfoliates the layered Co-based ZIF-L to prevent the serious aggregation of Co atoms and meanwhile preserves abundant N atoms to coordinate with them. Interestingly, with the assistance of molten salt, the coordinating N number of Co atom can be controlled by selectively introducing Zn evaporation to promote C–N fragments release. Then Co SACs with different N coordination numbers were used as

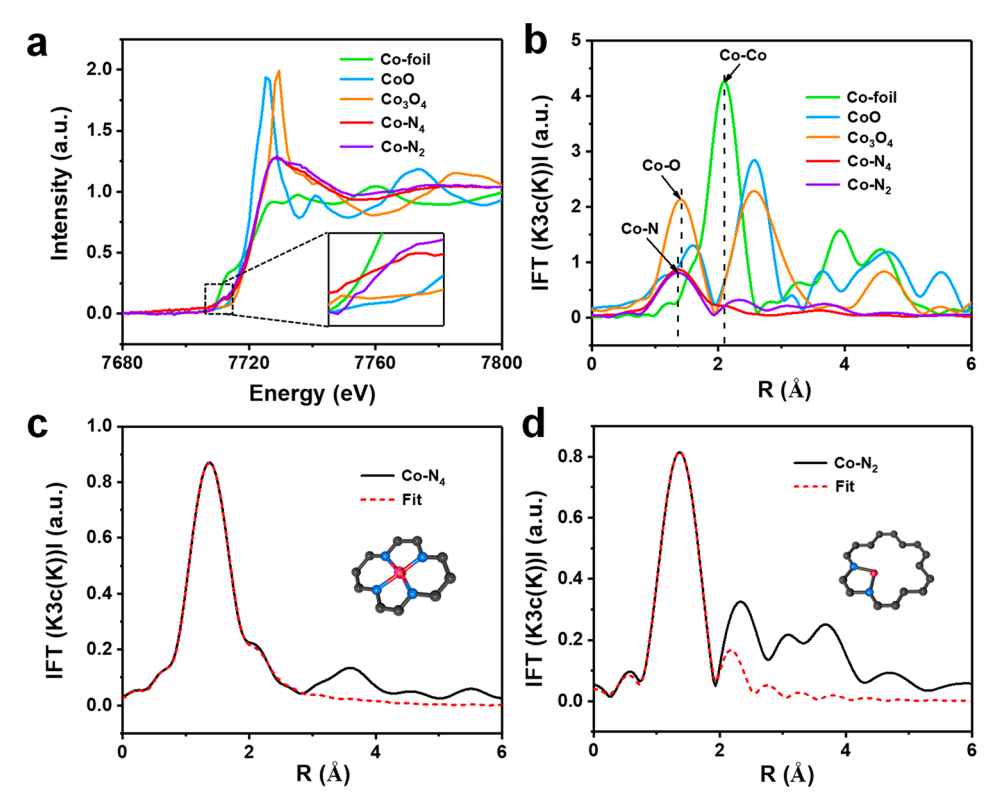


Figure 3. Atomic structure characterization. (a) Co K-edge XANES and (b) Fourier-transform EXAFS spectra of $Co-N_2$, and reference samples; the inset shows the pre-edge region. EXAFS fitting curves and optimized models of (c) $Co-N_4$ and (d) $Co-N_2$.

models to investigate the relationship between the M-N coordination environment and the LiPSs redox kinetics. Compared to Co-N₄, Co-N₂ exhibits enhanced chemical interaction with LiPSs and superior electrocatalytic effect on reaction kinetics of sulfur species, including both reduction and oxidation processes. Density functional theory (DFT) calculation further identifies that the outstanding electrocatalytic effect of Co-N2 on Li-S chemistry is derived from the synergistic effect of asymmetrical electron distribution of Co-N₂ moiety and increased unoccupied 3d orbitals of Co centers, which contributes to strengthen chemical interactions with LiPSs and promote interfacial charge transfer. As a result, Co-N₂ exhibits exceptional long-term cycling stability (0.05% capacity decay per cycle for 700 cycles) and excellent rate performance (687 mAh g⁻¹ at 5 C), exceeding Co-N₄. Even at a high S loading of 7.0 mg cm⁻², the battery with Co-N₂ modified separator achieves a high reversible capacity of 8.2 mAh cm⁻² and remains steady for 70 cycles at 0.1 C.

■ RESULTS AND DISCUSSION

As shown in the schematic illustration (Figure 1), Zn, Co-ZIF-L with layered structure was first mixed with LiCl and KCl salts and then heated at 800 °C under Ar protection. During the heating process, mobile Li⁺ and K⁺ ions in molten salt intercalated into the interlayers of Zn and Co-ZIF-L, and exfoliated the crystal layers, ^{29,30} where organic links were pyrolyzed into N-doped graphene (NG), which reduced Co and Zn nodes at the same time. ³¹ The intercalation-exfoliation process also helps to prevent the severe aggregation of Co atoms. Moreover, molten salt contributes to retaining abundant N elements on the graphene, ³² which firmly anchored the dispersed Co atoms by forming Co-N_x sites. ³³ Meanwhile, the in-situ-formed Zn nanoclusters with low

boiling point evaporated at 800 °C, 34 which created a large number of defects in the graphene and converted Co-N₄ into Co-N₂ by promoting volatile C-N fragments release. 25,35 After etching the Co nanoclusters with sulfuric acid, the graphene with abundant Co-N₂ sites was obtained (donated as Co-N₂). As a comparison, Co-N₄ and NG samples were also synthesized via similar methods, using Co-ZIF-L and Zn-ZIF-L as precursors, respectively. It should be noted that without Zn evaporation, Co-N₄ was obtained instead of Co-N₂. Thus, the key point to make Co SACs with different N coordination number is to combine molten-salt thermal exfoliation with defect-forming effect caused by Zn evaporation.

Scanning electron microscopy (SEM) and transmission electron microscopy (TEM) images confirm the graphene-like morphology of the obtained Co-N2 sample without metal nanoparticles (Figure 2a, as well as Figure S1 in the Supporting Information). High-resolution transmission electron microscopy (HRTEM) image shows that the graphene consists of crystal and amorphous domains (Figure S2). Selected-area electron diffraction (SAED) image in Figure 2a exhibits a ringlike diffraction pattern, indicating the polycrystalline feature of Co-N₂. Energy-dispersive X-ray spectroscopy (EDS) mapping result reveals that Co and N elements are well-distributed in the graphene (Figure 2b). Sphericalaberration-corrected STEM images show the well distribution of Co single atoms in the graphene (Figure 2c and 2d). X-ray photoelectron spectroscopy (XPS) was applied to analyze Co and N elements in detail. Except the typical peaks assigned to graphitic, pyrrolic, and pyridinic N groups, another peak at ~399.3 eV is found in XPS N 1s spectrum of Co-N₂ (Figure 2e), which can be attributed to the N_x -Co bond.³⁶ The XPS N 1s spectrum of $Co-N_4$ is similar to that of $Co-N_2$ (see

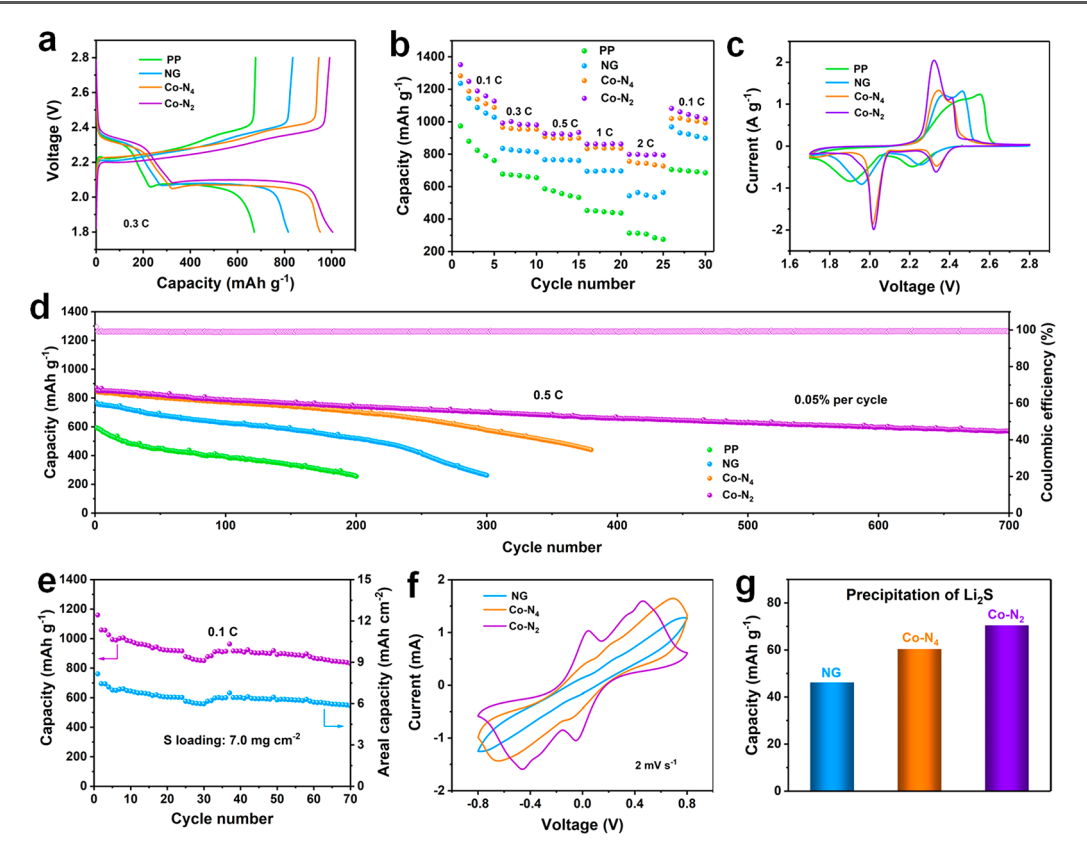


Figure 4. Electrochemical properties of Li-S batteries with unmodified PP, the NG, $Co-N_4$ or $Co-N_2$ modified separator: (a) charge–discharge curves; (b) rate performances; (c) CV profiles at 0.1 mV s⁻¹; (d) long-term cycling performances at 0.5 C; (e) cycling performance of Li-S battery with $Co-N_2$ modified separator at the sulfur loading of 7.0 mg cm⁻²; (f) CV curves of symmetrical cells with NG, $Co-N_4$, and $Co-N_2$ electrodes; and (g) comparison of capacities of Li₂S precipitation on NG, $Co-N_4$, and $Co-N_2$ substrates.

Figure S3a in the Supporting Information). While the N_x -Co bond does not exist in the XPS N 1s spectrum of NG (Figure S3b), the N content of Co-N₂ is 8.89 wt % (see Table S1 in the Supporting Information), which is much lower than that of Co-N₄ (12.88 wt%). The decrease of N content should derive from the release of C-N fragments promoted by Zn evaporation. High-resolution XPS Co 2p spectra of Co-N₄ exhibits two typical peaks at 796.4 and 781.1 eV, assigning to Co $2p_{1/2}$ and Co $2p_{3/2}$, respectively (Figure 2f). Compared with Co-N₄, the two peaks of Co-N₂ slightly shift to lower binding energies, suggesting the oxidation state decreased due to lower N coordinating number. 25 The weight percent of Co atoms in Co-N₂ and Co-N₄ sample is 2.52 and 2.63 wt %, respectively, via inductively coupled plasma optical emission spectroscopy (ICP-AES). The values are slightly higher than those tested by XPS (Table S1), which could be due to the fact that XPS mainly measures the surface information.³⁷ The X-ray diffraction (XRD) result of Co-N₂, Co-N₄, and NG possess the similar XRD patterns (Figure S4a in the Supporting Information), where only the peaks of carbon are observed. Raman spectra of the three samples (Figure S4b in the Supporting Information) all exhibit two typical peaks located at 1350 and 1580 cm⁻¹, which are assigned to D- and G-bands of carbon, respectively. And the ratio of $I_{\rm D}/I_{\rm G}$ in Co-N₂ is 1.09, which is the highest among the three samples, demonstrating that abundant defects exist in the Co-N2 sample. N₂ adsorption measurement (Figure S5 in the Supporting Information) illustrates that Co-N2 possesses a high BET (Brunauer-Emmett-Teller) specific surface area of 524 m² g⁻¹ with abundant micropores of <2 nm, which is

similar to that of $Co-N_4$ (529 m² g⁻¹). Such microporous structure with high specific surface area is beneficial for inhibiting the shuttle effect of LiPSs and exposing electrocatalytic active sites.

X-ray absorption near-edge structure (XANES) and extended X-ray absorption fine structure (EXAFS) measurements characterizes the chemical states and coordination environments of Co atoms in Co-N₂ and Co-N₄. As shown in Figure 3a, the adsorption edge positions of Co-N2 and Co-N₄ are located between that of Co-foil and CoO, demonstrating the average valence of Co of Co-N2 and Co-N₄ is the intermediate to Co⁰ and Co²⁺.³⁹ According to the inset of Figure 3a, Co-N₂ shows an increased pre-edge intensity, suggesting lower symmetry around Co atoms. 44 EXAFS spectra of both Co-N2 and Co-N4 exhibit a main peak at ~1.4 Å, which is assigned to Co-N coordination (Figure 3b). In addition, the Co-Co peak at ~ 2.1 Å from standard Co metal foil is absent in Co-N2 and Co-N4, which further proves that no cobalt nanoparticles or clusters exist in Co-N₂ and Co-N₄. 42 According to EXAFS fitting results (Figures 3c and 3d), the average Co-N coordination numbers of $Co-N_2$ and $Co-N_4$ is 2.2 and 3.7, respectively (Table S2 in the Supporting Information). This indicates that one Co atom in Co-N₄ mainly coordinates with four N atoms to form Co-N₄ site, as shown in the inset image of Figure 3c, while one Co atom in Co-N2 mainly coordinates with two N atoms to form Co-N₂ site. Considering abundant pores/defects existing in Co-N₂ and low symmetric coordination structure confirmed by XANES, it is likely that Co atoms are anchored by two

adjacent N atoms on the pores or defective edges, as shown in the inset image of Figure 3d.^{43,44}

Subsequently, Co-N2 was used to modify the commercial polypropylene (PP) separator by simple vacuum-filtration method. The cross-sectional SEM image exhibits the thickness of the coating layer is \sim 9.6 μ m with an areal loading of 0.23 mg cm⁻² (Figure S6a in the Supporting Information), and topsection SEM image reveals that the surface of PP separator is completely covered by Co-N₂ nanosheets (Figure S6b in the Supporting Information). Moreover, the Co-N₂ coating layer adheres to the separator tightly and can withstand the bending stress (Figure S7 in the Supporting Information). Co-N₄ and NG were also applied to modify the separators by using the similar method. The modified separators then were introduced into Li-S batteries to investigate their effects on the electrochemical properties by comparing with a pristine separator. Figure 4a shows the charge-discharge profiles of Li-S batteries with these separators at 0.3 C (1 C = 1675 mAh g^{-1}). The battery with Co-N₂ modified separator (Co-N₂/ PP) exhibits a higher discharge capacity (1004 mAh g⁻¹) than the batteries with PP (672 mAh g⁻¹), NG/PP (816 mAh g⁻¹), and Co-N₄/PP (951 mAh g⁻¹). In addition, the battery with Co-N₂/PP also has the smallest voltage hysteresis. The reversible capacities of Co-N₂/PP at 0.1, 0.3, 0.5, 1, and 2 C reach 1351, 1001, 934, 864, and 799 mAh g⁻¹, respectively, which are higher than the other control samples (Figure 4b), demonstrating superior rate performance of Co-N₂/PP. As the current density increases, the overpotential of Co-N₂/PP also gradually increases (see Figure S8 in the Suporting Information). Even at 2.0 C, the second plateau still can be observed, suggesting fast reaction kinetics. When the current density was further increased to 5 C, the capacity of Co-N₂/ PP still maintains 687 mAh g⁻¹ (Figure S9 in the Supporting Information). Meanwhile, at 5 C, the capacity of $Co-N_4/PP$ is only 501 mAh g⁻¹. With the current densities increasing, the capacity gap between Co-N₂/PP and Co-N₄/PP also increases, indicating that the electrocatalytic effect on accelerating reaction kinetics would be more obvious at higher current densities. 45,46 Cyclic voltammetry (CV) curves of the batteries with different separators at 0.1 mV s⁻¹ manifest four typical peaks: two anodic peaks and two cathodic peaks (Figure 4c). During the cathodic scan, the two cathodic peaks derive from the lithiation of sulfur to long-chain lithium polysulfides (Li₂S_x, $4 \le x \le 8$) and further reduction to shortchain sulfides (Li₂S₂ and Li₂S). During the subsequent anodic sweep, the two anodic peaks are ascribed to oxidation of shortchain sulfides to long-chain polysulfides and ultimately to sulfur.⁴⁷ Moreover, the polarization between anodic and cathodic peaks in CV curve of Co-N₂/PP is the smallest among the functional separators, which is consistent with charge-discharge curves. Besides, CV curve of Co-N₂/PP also possesses the highest current peak, suggesting the fastest LiPSs conversion induced by Co-N₂. As shown in Figure 4d, the long-term cycling performances of the cells with different separators were tested at 0.5 C. The cell with Co-N₂/PP exhibits an initial capacity of 871 mAh g⁻¹ and maintains a high capacity of 571 mAh g⁻¹ after 700 cycles with a low capacity decay rate of 0.05% per cycle and a high Coulombic efficiency of 99.5%. For comparison, the capacity of Co-N₄/ PP decayed to 439 mAh g⁻¹ after 380 cycles. In addition, the cycling stabilities of NG/PP and PP separators are even worse. In order to reveal the capacity contribution of Co-N₂ or Co- N_4 , the cycling performances of $Co-N_2$ and $Co-N_4$ electrodes

at 0.5 C were also tested as shown in Figure S10. The reversible capacities of both Co-N₂ and Co-N₄ are very low (<10 mAh g⁻¹), which indicates that the capacity contribution from Co-N2 or Co-N4 can be neglected. To further understand the outstanding cycling performance of the cell with Co-N₂/PP, the cycled batteries with different separators were disassembled to conduct a post analysis. The surface of the cycled lithium anode from the battery with Co-N₂/PP is much smoother than others (see Figure S11 in the Supporting Information), which demonstrates that few LiPSs get through the Co-N₂ modified separator to react with the lithium anode. The structure stability of Co-N₂ after cycling was also tested, as shown in Figure S12 in the Supporting Information. The graphene-like morphology is retained well and shows no difference to the original material. Besides, elemental Co is well-distributed in the carbon matrix. The excellent structure stability of Co-N2 contributes to achieve the long-term effect on improving the performance of Li-S batteries. To test the practical use of Co-N2 modified separator in lithium sulfur batteries with high-energy densities, the sulfur loading of cathode was further increased to 7.0 mg cm⁻² (Figure 4e). The areal capacity can reach 8.2 mAh cm⁻² at the beginning and maintain 5.9 mAh cm⁻² after 70 cycles at 0.1 C. The capacity fluctuations could derive from the volume fluctuations and redistribution of sulfur during cycling.⁴⁸ The electrochemical properties of the battery with Co-N2/PP are remarkable compared to previous related works (Table S3 in the Supporting Information). These results confirm that $Co-N_2$ efficiently immobilizes LiPSs and catalyzes their conversion.

To further investigate the catalytic effect of Co-N₂ on LiPSs conversion, the symmetric cell was assembled by using Co-N2 as identical electrodes. For comparison, the symmetric cell with Co-N₄ and NG as identical electrodes were also assembled. As shown in Figure 4f, the CV curve of Co-N₂ electrode exhibits two obvious reduction peaks at -0.05 and -0.46 eV, and two distinct oxidation peaks at 0.05 and 0.46 eV. The two reduction peaks correspond to the conversion of Li₂S₆ to short-chain LiPSs and Li₂S, respectively. Meanwhile, the two oxidation peaks are derived from the oxidation of Li₂S to LiPSs and S. 42 In contrast, the Co-N₄ electrode shows only one pair of peaks and the NG electrode does not even have any obvious redox peaks. Besides, the current peaks of Co-N₂ electrode are also the highest among the three types of electrodes. The CV curves demonstrate that Co-N₂ possesses a higher catalytic activity for the LiPSs conversion than Co-N₄ and NG. Electrochemical impedance spectroscopy (EIS) of the symmetric cells also reveals that Co-N₂ shows the smallest charge-transfer resistance (Figure S13 in the Supporting Information), suggesting the fastest interfacial charge transfer. To investigate the effects of these materials on the Li₂S nucleation, the Li₂S nucleation test was performed. During the potentiostatic (2.07 V) discharge process, Li₂S would nucleate and grow on these materials. 49 As shown in Figure S14 in the Supporting Information, the Co-N₂ electrode shows a higher discharging current peak than Co-N₄ and NG electrodes. In addition, the capacity of Li₂S precipitation on Co-N₂ electrode is 70.5 mAh g^{-1} in Figure 4g, which is higher than $Co-N_4$ (60.4 mAh g^{-1}) and NG electrode (46.2 mAh g^{-1}), indicating Co-N2 can also effectively accelerate the liquidsolid conversion process. Considering the Li₂S decomposition process also has great influence on the battery performance, the role of Co-N₂ on the dissolution kinetics of Li₂S was further evaluated by analyzing the Tafel slope and the initial

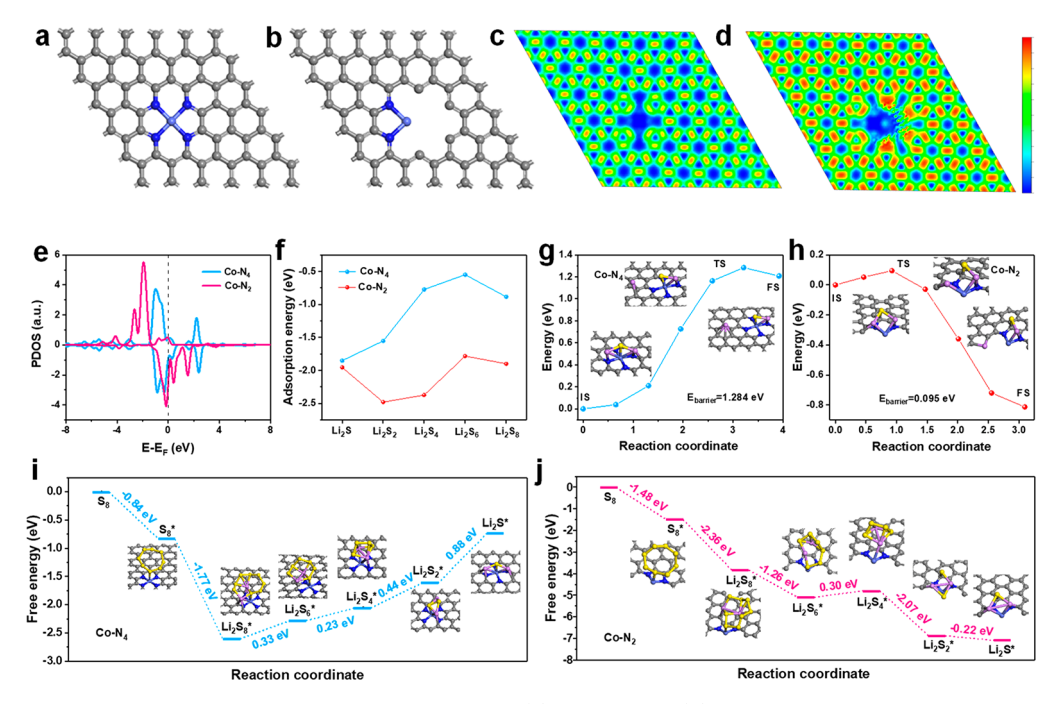


Figure 5. Theoretical calculations. Illustration of local structures of (a) $Co-N_4$ and (b) $Co-N_2$ applied in DFT calculation. (c, d) Charge density differences of $Co-N_4$ (panel (c)) and $Co-N_2$ (panel (d)), the red and blue represents electron accumulation and depletion, respectively. (e) Partial density of states (PDOS) of Co d-orbital in $Co-N_4$ and $Co-N_2$. (f) Adsorption energies of $Co-N_4$ and $Co-N_2$ for Li_2S_8 , Li_2S_6 , Li_2S_4 , Li_2S_2 , and Li_2S . Decomposition energy barriers of $Co-N_4$ and (h) $Co-N_2$. Energy profiles for the reduction of $Co-N_4$ and (j) $Co-N_4$ and (j) $Co-N_4$ substrates.

charge curve, as shown in Figure S15 in the Supporting Information. The Li-S battery with $Co-N_2$ modified separator shows smaller Tafel slope of the charge process than the batteries with NG and $Co-N_2$ modified separators (Figure S15a in the Supporting Information), which implies faster Li₂S oxidization on $Co-N_2$. Besides, the initial charge profiles in Figure S15b in the Supporting Information also exhibit that the battery with $Co-N_2$ modified separator possesses the smallest overpotential, indicating that $Co-N_2$ is more favorable for catalyzing the oxidation of Li₂S.

Density functional theory (DFT) calculation was applied to further explore the mechanism behind the superior performance of Co-N2 at the atomic level. The local structures of Co-N₄ and Co-N₂ applied in DFT calculation are depicted in Figures 5a and 5b, consistent with the experimental observations. The charge density difference of Co-N₄ possesses a perfectly symmetric electron structure (Figure 5c). While in Co-N₂ moiety, the charge distribution is asymmetrical (Figure 5d). The asymmetrical electron distribution can endow the Co-N₂ moiety with stronger polarity to anchor LiPSs through polar-polar interaction. In Figure 5e, the PDOS analysis reveals that the decreased N coordination number also makes the d-band center of the active center Co atom upshift from -0.85 eV (Co $-N_4$) to -0.55 eV (Co $-N_2$). The upward-shifted d-band center leads to decreasing occupation states of 3d orbits in Co atom, 25 which benefits the Lewis acid-base interaction between Co atoms and S_n²⁻ of LiPSs. To reveal the influence of the unique electronic structure of Co-N2 on the adsorption ability of LiPSs, the adsorption energies of Co-N2 and Co-N4 for various LiPSs were calculated and shown in Figure 5f.²⁷ The adsorption energies of different LiPSs on Co-N2 are higher than that on Co-N₄, which endows Co-N₂ with enhanced adsorption ability for LiPSs, which is further confirmed by the adsorption

experiment in Figure S16 in the Supporting Information. As shown in Figure S17, XPS was applied to investigate the interaction between Co-N₂ and LiPSs. After adsorbing Li₂S₆, the Co 2p peaks shift to lower binding energy, indicating the strong chemical interaction between Co atoms and Li₂S₆. To understand the effect of electron structure differences on the LiPSs reduction, the Gibbs free energies of the above main reduction products with optimized structures on Co-N₄ or Co-N₂ were modeled (Figures 5i and 5j). The difference of Gibbs free energies of nearby LiPSs (defined as ΔE) can reflect the reaction speed of each conversion step: the lower ΔE values means the faster reaction kinetics. 21 Except the conversion of Li₂S₆ into Li₂S₄, the E values of other reaction steps on $Co-N_2$ are much lower than those on $Co-N_4$, which means that other reaction steps on Co-N2 are more thermodynamically favorable than on Co-N₄. Besides, for $Co-N_2$, the formation of Li_2S_4 from Li_2S_6 possesses the largest positive Gibbs free energy of 0.30 eV, indicating that it is the rate-limiting step. Meanwhile, for Co-N₄, the formation of Li₂S from Li₂S₂ is the rate-limiting step, which has a much higher Gibbs free energy (0.88 eV), further confirming that Co-N₂ is more effective for catalyzing LiPSs reduction. 50 In addition, to evaluate the reaction kinetics of the charging process on the surfaces of Co-N₄ and Co-N₂, the energy barriers of Li₂S decomposition on Co-N₄ and Co-N₂ substrates were also calculated (Figures 5g and 5h). The energy barrier of Li₂S decomposition on Co-N₂ is only 0.095 eV, much lower than that on $Co-N_4$ (1.28 eV). This confirms that Li₂S is much easier to be oxidized into LiPSs on Co-N₂ during the charging process, which is beneficial for improving S utilization. 51 The above results demonstrate that the asymmetrical electron structure of Co atoms with upshift d-band center caused by the low N coordination number endows Co-

N₂ with stronger chemical interaction with LiPSs and superior catalytic effect on LiPSs conversion versus Co-N₄.

CONCLUSION

In summary, an exfoliation-evaporation strategy assisted by molten salt is proposed to synthesize Co SACs with different N coordination number by using Co-based ZIF-L with layered structure as precursors. The key of this unique strategy is to combine molten-salt thermal exfoliation with the defectforming effect caused by Zn evaporation. The as-prepared Co SACs with different N coordination numbers were used as the model to investigate the relationship between Co-N coordination-number determined electron structure and LiPSs redox kinetics. DFT calculation and experiments reveal that decreasing the N coordination number breaks the symmetric electronic distribution and upshifts the d-band center of the active center Co atom, which leads to that Co-N2 achieves stronger chemical interaction with LiPSs and accelerates LiPSs redox kinetics more efficiently than Co-N₄. Therefore, the Li-S batteries with Co-N₂ modified separators exhibit outstanding electrochemical properties even at a high loading of 7.0 mg cm^{-2} .

METHODS

Preparation of Co, Zn-ZIF-L, Co-ZIF-L, and Zn-ZIF-L. First, 2.60 g of 2-methylimidazole (2-MIM) was dissolved in 80 mL of deionized (DI) water to obtain solution A. Meanwhile, 0.585 g of Co(NO₃)₂·6H₂O and 0.595 g of Zn(NO₃)₂·6H₂O were dissolved in 80 mL of DI water to obtain solution B. Then, solution B was poured into solution A under agitation. After being kept for 4 h under room temperature, the mixture solution was centrifuged and cleaned with DI water three times and finally dried at 80 °C overnight. For the preparation of Co-ZIF-L, the same method as that used for Co, Zn-ZIF-L was conducted, except for using 1.17 g of Co(NO₃)₂·6H₂O without Zn(NO₃)₂·6H₂O was used. For preparation of Zn-ZIF-L, the same method as that used for Co, Zn-ZIF-L was conducted, except for using 1.19 g Zn(NO₃)₂·6H₂O without Co(NO₃)₂·6H₂O.

Preparation of Co–N₂, Co–N₄, and NG. The asprepared Co, Zn-ZIF-L was mixed with 2.0 g LiCl and 8.0 g KCl by grounding. The mixture then was heated under Ar protection to 400 °C for 2 h with a heating rate of 2 °C/min and then was increased to 800 °C with the same heating rate and maintained for another 2 h. After cooling, the product was washed with 1.0 M H₂SO₄ solution, to remove the impurities. Finally, the product was washed with DI water several times until the solution pH reached 7.0 and then it was dried in an oven at 80 °C overnight to get Co–N₂. Co–N₄ and NG were prepared using a similar method, except Co-ZIF-L and Zn-ZIF-L were used as precursors, respectively.

Preparation of Co–N₂, Co–N₄, and NG Modified Separators. Co–N₂ (3.0 mg) was added into 20 mL of ethanol and then sonicated for 0.5 h to obtain the well-distributed suspension, which was vacuum-filtered through the PP separator. After being dried at 50 °C overnight, the Co–N₂ modified separator was obtained. The areal loading amount of the coating layer was \sim 0.23 mg cm⁻². Co–N₄ and NG modified separators were prepared by using the same method, except 3.0 mg of Co–N₄ and 3.0 mg of NG, respectively, were used.

Preparation of Blank Electrolyte, Li₂S₆ and Li₂S₈ Catholyte. The blank electrolyte was made by dissolving 1.0 M LiTFSI and 2 wt % LiNO₃ into DOL/DME (1:1 by volume). The Li₂S₆ or Li₂S₈ catholyte was produced by adding S and Li₂S powders (5:1 or 7:1 by weight) into the blank electrolyte and continuously stirred in argon-filled glovebox for 12 h.

Assembly of the Symmetric Cell. The ${\rm Co-N_2}$ ${\rm Co-N_4}$, or NG composite mixed with PVDF binder (mass ratio of 80:20) was subsequently coated onto aluminum foil (areal loading of 0.4 mg cm⁻²). A symmetric cell using these composites as an identical counter and working electrodes was prepared with the 20 μ L 0.2 M Li₂S₆ electrolyte.

Measurement for the Li₂S Nucleation. Lithium foil was used as an anode and the above composite electrodes were used as cathodes. Then, 20 μ L of Li₂S₈ (0.2 M) catholyte and 20 μ L of electrolyte without Li₂S₈ anolyte was injected into the cell. The cell was first galvanostatically discharged under a current of 0.112 mA until the voltage reduced to 2.08 V, then maintained at 2.07 V for Li₂S nucleation and growth.

Materials Characterization. The morphology and microstructure were measured by scanning electron microscopy (SEM) (JEOL, Model JSM-7600F) and transmission electron microscopy (TEM) (JEOL, Model JEM-2100F). High-angle annular dark-field scanning transmission electron microscopy (HAADF-STEM) images were obtained by using a JEOL Model JEM-ARF200F TEM/STEM equipped with a spherical aberration corrector. The X-ray diffraction (XRD) patterns of the materials were measured by a Bruker D8 Avance X-ray diffractometer equipped with Cu K α radiation ($\lambda = 0.154$ nm) source. X-ray photoelectron spectroscopy (XPS) tests were performed by an XPS instrument (PHI, Model 5600) with monochromatic Al Ka X-rays (350 W) and a pass energy of 29 eV. Nitrogen adsorption and desorption isotherms were obtained on an automated gas sorption analyzer (Autolab-iQ, Quantachrome Instruments) determined by the BET method. Raman spectra were collected by a confocal Raman system (WITec Instruments Corp., Germany) with a 532 nm excitation laser. Co K-edge XAS was measured at Wiggler Beamline BL17C1 of Taiwan Light Source (TLS) at the National Synchrotron Radiation Research Center (NSRRC).

Electrochemical Measurements. The rechargeable Li–S batteries with PP, Co-N2, Co-N4 or NG separator were tested in CR2025 coin-type cells. Sulfur cathodes were obtained by mixing commercial sulfur and Ketjen Black (KB) with a mass ratio of 7:3. The above mixture was transferred to 50 mL Teflon-lined stainless-steel autoclave under an argon-filled glovebox and heated at 155 °C for 15 h. The blend of S/KB mixture, CMC binder, and KB then were mixed in deionized water with a mass ratio of 8:1:1. The slurry then was coated onto Al current collector with the areal sulfur loading of ~1.0 mg cm⁻². For comparison, thicker sulfur cathodes with higher areal sulfur loading of 7.0 mg cm⁻² were also prepared. The electrolyte/sulfur ratios were 17.7 and 7.3 $\mu L/mg$ for low- and high-sulfur-loading cells. The S/KB material was used as the cathode and lithium foil was employed as the anode. 1.0 M LiTFSI in DME/DOL (v/v = 1:1) (20 μ L) with 2 wt % LiNO₃ was used as an electrolyte. The galvanostatic charge-discharge measurements were performed on a Neware battery testing system. The cyclic voltammetry and electrochemical impedance spectroscopy were tested by a VMP3 electrochemical workstation. The specific capacities were calculated according to the weight/mass of sulfur.

Details of First-Principles Calculations. The Vienna Ab initio Simulation Package (VASP) was employed to perform all density functional theory (DFT) calculations within the generalized gradient approximation (GGA), using the Perdew–Burke–Ernzerhof (PBE) functional. The projected augmented wave (PAW) potentials were chosen to describe the ionic cores and take valence electrons into account, using a plane wave basis set with a kinetic energy cutoff of 400 eV. The DFT-D3 empirical correction method was used to describe van der Waals interactions. Geometry optimizations were performed with a force convergency of <0.05 eV/Å. The original bulk structures of $Co-N_4$ and $Co-N_2$ have been optimized before the construction of surfaces with the Monkhorst–Pack k-point of $1 \times 1 \times 1$. The adsorption energy was calculated with the equation

$$E_{\text{ads}} = E(\text{Li}_2 S_x / \text{substrate}) - E(\text{Li}_2 S_x) - E(\text{substrate})$$

with x = 1, 2, 4, 6, and 8. The barriers for Li₂S decomposition on Co-N₄ and Co-N₂ were calculated with the climbing-image nudged elastic band (CI-NEB) method, to evaluate delithiation reaction kinetics.

ASSOCIATED CONTENT

Supporting Information

The Supporting Information is available free of charge at https://pubs.acs.org/doi/10.1021/acsmaterialslett.1c00414.

Experimental methods, TEM images, SEM images, N₂ adsorption—desorption, pore size distribution, Raman spectrum, XRD patterns, CV curves, galvanostatic discharge/charge curves, elemental mappings, XPS spectra, and performance comparison (PDF)

AUTHOR INFORMATION

Corresponding Author

Hui Ying Yang — Pillar of Engineering Product Development, Singapore University of Technology and Design, Singapore 487372, Singapore; orcid.org/0000-0002-2244-8231; Email: yanghuiying@sutd.edu.sg

Authors

Daliang Fang – Pillar of Engineering Product Development, Singapore University of Technology and Design, Singapore 487372, Singapore

Pan Sun – NSF'S ChemMatCARS, University of Chicago, Chicago, Illinois 60637, United States

Shaozhuan Huang – Key Laboratory of Catalysis and Energy Materials Chemistry of Ministry of Education, South-Central University for Nationalities, Wuhan, Hubei 430074, China

Yang Shang — Pillar of Engineering Product Development, Singapore University of Technology and Design, Singapore 487372, Singapore

Xueliang Li — Pillar of Engineering Product Development, Singapore University of Technology and Design, Singapore 487372, Singapore

Dong Yan — Pillar of Engineering Product Development, Singapore University of Technology and Design, Singapore 487372, Singapore

Yew Von Lim — Pillar of Engineering Product Development, Singapore University of Technology and Design, Singapore 487372, Singapore

Ching-Yuan Su — Department of Mechanical Engineering, Graduate Institute of Energy Engineering, and Graduate, Institute of Material Science and Engineering, National Central University, Tao-Yuan 32001 Taiwan, Republic of China; orcid.org/0000-0001-9295-7587

Bing-Jian Su — Department of Electrophysics, National Chiao Tung University, Hsinchu 30010 Taiwan, Republic of China; orcid.org/0000-0002-1785-4518

Jenh-Yih Juang — Department of Electrophysics, National Chiao Tung University, Hsinchu 30010 Taiwan, Republic of China

Complete contact information is available at: https://pubs.acs.org/10.1021/acsmaterialslett.1c00414

Notes

The authors declare no competing financial interest.

ACKNOWLEDGMENTS

The research project is supported by the Ministry of Education, Singapore, under its MOE tier2 grant (No. MOE2019-T2-1-181). This work is also supported by National Science Foundation (No. NSF/CHE-1834750).

REFERENCES

- (1) Manthiram, A.; Fu, Y.; Chung, S. H.; Zu, C.; Su, Y. S. Rechargeable lithium-sulfur batteries. *Chem. Rev.* **2014**, *114*, 11751–87.
- (2) Salama, M.; Rosy Attias, R.; Yemini, R.; Gofer, Y.; Aurbach, D.; Noked, M. Metal—sulfur batteries: overview and research methods. *ACS Energy Lett.* **2019**, *4*, 436–446.
- (3) Wild, M.; O'Neill, L.; Zhang, T.; Purkayastha, R.; Minton, G.; Marinescu, M.; Offer, G. J. Lithium sulfur batteries, a mechanistic review. *Energy Environ. Sci.* **2015**, *8*, 3477–3494.
- (4) Zhang, M.; Chen, W.; Xue, L.; Jiao, Y.; Lei, T.; Chu, J.; Huang, J.; Gong, C.; Yan, C.; Yan, Y.; Hu, Y.; Wang, X.; Xiong, J. Adsorption Catalysis Design in the Lithium Sulfur Battery. *Adv. Energy Mater.* **2020**, *10*, 1903008.
- (5) Chung, S.-H.; Luo, L.; Manthiram, A. TiS2—polysulfide hybrid cathode with high sulfur loading and low electrolyte consumption for lithium—sulfur batteries. *ACS Energy Lett.* **2018**, *3*, 568—573.
- (6) Gu, X.-X.; Yang, Z.-G.; Qiao, S.; Shao, C.-B.; Ren, X.-L.; Yang, J.-J. Exploiting methylated amino resin as a multifunctional binder for high-performance lithium—sulfur batteries. *Rare Met.* **2021**, *40*, 529—536.
- (7) Han, X.-R.; Guo, X.-T.; Xu, M.-J.; Pang, H.; Ma, Y.-W. Clean utilization of palm kernel shell: sustainable and naturally heteroatom-doped porous activated carbon for lithium—sulfur batteries. *Rare Met.* **2020**, *39*, 1099—1106.
- (8) Wang, Y.; Zhang, R.; Chen, J.; Wu, H.; Lu, S.; Wang, K.; Li, H.; Harris, C. J.; Xi, K.; Kumar, R. V.; Ding, S. Enhancing Catalytic Activity of Titanium Oxide in Lithium—Sulfur Batteries by Band Engineering. *Adv. Energy Mater.* **2019**, *9*, 1900953.
- (9) Luo, L.; Li, J.; Yaghoobnejad Asl, H.; Manthiram, A. In-situ assembled VS4 as a polysulfide mediator for high-loading lithium—sulfur batteries. *ACS Energy Lett.* **2020**, *5*, 1177–1185.
- (10) Yuan, H.; Peng, H.-J.; Li, B.-Q.; Xie, J.; Kong, L.; Zhao, M.; Chen, X.; Huang, J.-Q.; Zhang, Q. Conductive and Catalytic Triple-Phase Interfaces Enabling Uniform Nucleation in High-Rate Lithium-Sulfur Batteries. *Adv. Energy Mater.* **2019**, *9*, 1802768.
- (11) Jeong, T.-G.; Choi, D. S.; Song, H.; Choi, J.; Park, S.-A.; Oh, S. H.; Kim, H.; Jung, Y.; Kim, Y.-T. Heterogeneous catalysis for lithium—sulfur batteries: enhanced rate performance by promoting polysulfide fragmentations. *ACS energy Lett.* **2017**, *2*, 327–333.
- (12) Wang, Z.; Shen, J.; Liu, J.; Xu, X.; Liu, Z.; Hu, R.; Yang, L.; Feng, Y.; Liu, J.; Shi, Z.; Ouyang, L.; Yu, Y.; Zhu, M. Self-Supported and Flexible Sulfur Cathode Enabled via Synergistic Confinement for High-Energy-Density Lithium-Sulfur Batteries. *Adv. Mater.* **2019**, *31*, 1902228.

- (13) Lu, C.; Fang, R.; Chen, X. Single-Atom Catalytic Materials for Advanced Battery Systems. *Adv. Mater.* **2020**, 32, 1906548.
- (14) Zang, W.; Kou, Z.; Pennycook, S. J.; Wang, J. Heterogeneous Single Atom Electrocatalysis, Where "Singles" Are "Married. *Adv. Energy Mater.* **2020**, *10*, 1903181.
- (15) Kou, Z.; Zang, W.; Wang, P.; Li, X.; Wang, J. Single atom catalysts: a surface heterocompound perspective. *Nanoscale Horiz.* **2020**, *5*, 757–764.
- (16) Zhao, C.; Xu, G. L.; Yu, Z.; Zhang, L.; Hwang, I.; Mo, Y. X.; Ren, Y.; Cheng, L.; Sun, C. J.; Ren, Y.; Zuo, X.; Li, J. T.; Sun, S. G.; Amine, K.; Zhao, T. A high-energy and long-cycling lithium-sulfur pouch cell via a macroporous catalytic cathode with double-end binding sites. *Nat. Nanotechnol.* **2021**, *16*, 166–173.
- (17) Liu, Y.; Wei, Z.; Zhong, B.; Wang, H.; Xia, L.; Zhang, T.; Duan, X.; Jia, D.; Zhou, Y.; Huang, X. O-, N-Coordinated single Mn atoms accelerating polysulfides transformation in lithium-sulfur batteries. *Energy Storage Mater.* **2021**, *35*, 12–18.
- (18) Wang, F.; Li, J.; Zhao, J.; Yang, Y.; Su, C.; Zhong, Y. L.; Yang, Q.-H.; Lu, J. Single-Atom Electrocatalysts for Lithium Sulfur Batteries: Progress, Opportunities, and Challenges. *ACS Mater. Lett.* **2020**, *2*, 1450–1463.
- (19) Lu, C.; Chen, Y.; Yang, Y.; Chen, X. Single-atom Catalytic Materials for Lean-electrolyte Ultrastable Lithium-Sulfur Batteries. *Nano Lett.* **2020**, *20*, 5522–5530.
- (20) Xie, J.; Li, B. Q.; Peng, H. J.; Song, Y. W.; Zhao, M.; Chen, X.; Zhang, Q.; Huang, J. Q. Implanting Atomic Cobalt within Mesoporous Carbon toward Highly Stable Lithium-Sulfur Batteries. *Adv. Mater.* **2019**, *31*, 1903813.
- (21) Zhang, L.; Liu, D.; Muhammad, Z.; Wan, F.; Xie, W.; Wang, Y.; Song, L.; Niu, Z.; Chen, J. Single Nickel Atoms on Nitrogen-Doped Graphene Enabling Enhanced Kinetics of Lithium-Sulfur Batteries. *Adv. Mater.* **2019**, *31*, 1903955.
- (22) Zhang, K.; Chen, Z.; Ning, R.; Xi, S.; Tang, W.; Du, Y.; Liu, C.; Ren, Z.; Chi, X.; Bai, M.; Shen, C.; Li, X.; Wang, X.; Zhao, X.; Leng, K.; Pennycook, S. J.; Li, H.; Xu, H.; Loh, K. P.; Xie, K. Single-Atom Coated Separator for Robust Lithium-Sulfur Batteries. ACS Appl. Mater. Interfaces 2019, 11, 25147–25154.
- (23) Chen, K.; Liu, K.; An, P.; Li, H.; Lin, Y.; Hu, J.; Jia, C.; Fu, J.; Li, H.; Liu, H.; Lin, Z.; Li, W.; Li, J.; Lu, Y. R.; Chan, T. S.; Zhang, N.; Liu, M. Iron phthalocyanine with coordination induced electronic localization to boost oxygen reduction reaction. *Nat. Commun.* 2020, 11, 4173.
- (24) Shen, H.; Gracia-Espino, E.; Ma, J.; Tang, H.; Mamat, X.; Wagberg, T.; Hu, G.; Guo, S. Atomically FeN₂ moieties dispersed on mesoporous carbon: A new atomic catalyst for efficient oxygen reduction catalysis. *Nano Energy* **2017**, *35*, 9–16.
- (25) Wang, X.; Chen, Z.; Zhao, X.; Yao, T.; Chen, W.; You, R.; Zhao, C.; Wu, G.; Wang, J.; Huang, W.; Yang, J.; Hong, X.; Wei, S.; Wu, Y.; Li, Y. Regulation of Coordination Number over Single Co Sites: Triggering the Efficient Electroreduction of CO₂. Angew. Chem., Int. Ed. 2018, 57, 1944–1948.
- (26) Qiu, Y.; Fan, L.; Wang, M.; Yin, X.; Wu, X.; Sun, X.; Tian, D.; Guan, B.; Tang, D.; Zhang, N. Precise Synthesis of Fe-N₂ Sites with High Activity and Stability for Long-Life Lithium-Sulfur Batteries. *ACS Nano* **2020**, *14*, 16105–16113.
- (27) Ma, F.; Wan, Y.; Wang, X.; Wang, X.; Liang, J.; Miao, Z.; Wang, T.; Ma, C.; Lu, G.; Han, J.; Huang, Y.; Li, Q. Bifunctional Atomically Dispersed Mo-N₂/C Nanosheets Boost Lithium Sulfide Deposition/Decomposition for Stable Lithium-Sulfur Batteries. *ACS Nano* **2020**, *14*, 10115–10126.
- (28) Chen, Y.; Gao, R.; Ji, S.; Li, H.; Tang, K.; Jiang, P.; Hu, H.; Zhang, Z.; Hao, H.; Qu, Q.; Liang, X.; Chen, W.; Dong, J.; Wang, D.; Li, Y. Atomic-level modulation of electronic density at Co single-atom sites derived from metal-organic frameworks: enhanced oxygen reduction performance. *Angew. Chem., Int. Ed.* **2021**, *60*, 3212–3221.
- (29) Liu, X.; Antonietti, M. Moderating black powder chemistry for the synthesis of doped and highly porous graphene nanoplatelets and their use in electrocatalysis. *Adv. Mater.* **2013**, *25*, 6284–90.

- (30) Motevalli, B.; Taherifar, N.; Wang, H.; Liu, J. Z. Ab Initio Simulations To Understand the Leaf-Shape Crystal Morphology of ZIF-L with Two-Dimensional Layered Network. *J. Phys. Chem. C* **2017**, 121, 2221–2227.
- (31) Yin, P.; Yao, T.; Wu, Y.; Zheng, L.; Lin, Y.; Liu, W.; Ju, H.; Zhu, J.; Hong, X.; Deng, Z.; Zhou, G.; Wei, S.; Li, Y. Single Cobalt Atoms with Precise N-Coordination as Superior Oxygen Reduction Reaction Catalysts. *Angew. Chem., Int. Ed.* **2016**, *55*, 10800–5.
- (32) Hou, Y. N.; Zhao, Z.; Yu, Z.; Tang, Y.; Wang, X.; Qiu, J. Two-dimensional graphene-like N, Co-codoped carbon nanosheets derived from ZIF-67 polyhedrons for efficient oxygen reduction reactions. *Chem. Commun.* **2017**, *53*, 7840–7843.
- (33) Gong, Y. N.; Jiao, L.; Qian, Y.; Pan, C. Y.; Zheng, L.; Cai, X.; Liu, B.; Yu, S. H.; Jiang, H. L. Regulating the Coordination Environment of MOF-Templated Single-Atom Nickel Electrocatalysts for Boosting CO2 Reduction. *Angew. Chem., Int. Ed.* **2020**, *59*, 2705–2709
- (34) Wang, Z.; Huang, J.; Guo, Z.; Dong, X.; Liu, Y.; Wang, Y.; Xia, Y. A Metal-Organic Framework Host for Highly Reversible Dendrite-free Zinc Metal Anodes. *Joule* **2019**, *3*, 1289–1300.
- (35) Lee, J.-H.; Kim, R.; Kim, S.; Heo, J.; Kwon, H.; Yang, J. H.; Kim, H.-T. Dendrite-free Zn electrodeposition triggered by interatomic orbital hybridization of Zn and single vacancy carbon defects for aqueous Zn-based flow batteries. *Energy Environ. Sci.* **2020**, 13, 2839–2848.
- (36) Tang, C.; Wang, B.; Wang, H. F.; Zhang, Q. Defect Engineering toward Atomic Co-Nx -C in Hierarchical Graphene for Rechargeable Flexible Solid Zn-Air Batteries. *Adv. Mater.* **2017**, *29*, 1703185.
- (37) Yan, D.; Huang, S.; Von Lim, Y.; Fang, D.; Shang, Y.; Pam, M. E.; Yu, J.; Xiong, D.; Li, X. L.; Zhang, J.; Wang, Y.; Pan, L.; Bai, Y.; Shi, Y.; Yang, H. Y. Stepwise Intercalation-Conversion-Intercalation Sodiation Mechanism in CuInS2 Prompting Sodium Storage Performance. ACS Energy Lett. 2020, 5, 3725–3732.
- (38) Fang, D.; Chen, S.; Wang, X.; Bando, Y.; Golberg, D.; Zhang, S. ZnS quantum dots@multilayered carbon: geological-plate-movement-inspired design for high-energy Li-ion batteries. *J. Mater. Chem. A* **2018**, *6*, 8358–8365.
- (39) Zhu, W.; Zhang, L.; Liu, S.; Li, A.; Yuan, X.; Hu, C.; Zhang, G.; Deng, W.; Zang, K.; Luo, J.; Zhu, Y.; Gu, M.; Zhao, Z. J.; Gong, J. Enhanced CO2 Electroreduction on Neighboring Zn/Co Monomers by Electronic Effect. *Angew. Chem., Int. Ed.* **2020**, *59*, 12664–12668. (40) Li, J.; Zhang, H.; Samarakoon, W.; Shan, W.; Cullen, D. A.; Karakalos, S.; Chen, M.; Gu, D.; More, K. L.; Wang, G.; Feng, Z.; Wang, Z.; Wu, G. Thermally Driven Structure and Performance Evolution of Atomically Dispersed FeN₄ Sites for Oxygen Reduction. *Angew. Chem., Int. Ed.* **2019**, *58*, 18971–18980.
- (41) Li, Y.; Wu, J.; Zhang, B.; Wang, W.; Zhang, G.; Seh, Z. W.; Zhang, N.; Sun, J.; Huang, L.; Jiang, J.; Zhou, J.; Sun, Y. Fast conversion and controlled deposition of lithium polysulfides in lithium-sulfur batteries using high-loading cobalt single atoms. *Energy Storage Mater.* **2020**, *30*, 250–259.
- (42) Du, Z.; Chen, X.; Hu, W.; Chuang, C.; Xie, S.; Hu, A.; Yan, W.; Kong, X.; Wu, X.; Ji, H.; Wan, L.-J. Cobalt in Nitrogen-Doped Graphene as Single-Atom Catalyst for High-Sulfur Content Lithium-Sulfur Batteries. *J. Am. Chem. Soc.* **2019**, *141*, 3977–3985.
- (43) Guan, A.; Chen, Z.; Quan, Y.; Peng, C.; Wang, Z.; Sham, T.-K.; Yang, C.; Ji, Y.; Qian, L.; Xu, X.; Zheng, G. Boosting ${\rm CO_2}$ Electroreduction to ${\rm CH_4}$ via Tuning Neighboring Single-Copper Sites. ACS Energy Lett. 2020, 5, 1044–1053.
- (44) Wang, Y.; Adekoya, D.; Sun, J.; Tang, T.; Qiu, H.; Xu, L.; Zhang, S.; Hou, Y. Manipulation of Edge-Site Fe-N-2 Moiety on Holey Fe, N Codoped Graphene to Promote the Cycle Stability and Rate Capacity of Li-S Batteries. *Adv. Funct. Mater.* **2019**, 29, 1807485.
- (45) Fang, D.; Wang, G.; Huang, S.; Chen Li, T.; Yu, J.; Xiong, D.; Yan, D.; Liang Li, X.; Zhang, J.; Von Lim, Y.; Yang, S. A.; Ying Yang, H. Combination of heterostructure with oxygen vacancies in Co@ CoO_{1-x} nanosheets array for high-performance lithium sulfur batteries. *Chem. Eng. J.* **2021**, *411*, 128546.

- (46) Zhou, G.; Zhao, S.; Wang, T.; Yang, S. Z.; Johannessen, B.; Chen, H.; Liu, C.; Ye, Y.; Wu, Y.; Peng, Y.; Liu, C.; Jiang, S. P.; Zhang, Q.; Cui, Y. Theoretical Calculation Guided Design of Single-Atom Catalysts toward Fast Kinetic and Long-Life Li-S Batteries. *Nano Lett.* 2020, 20, 1252–1261.
- (47) Fan, S.; Huang, S.; Pam, M. E.; Chen, S.; Wu, Q.; Hu, J.; Wang, Y.; Ang, L. K.; Yan, C.; Shi, Y.; Yang, H. Y. Design Multifunctional Catalytic Interface: Toward Regulation of Polysulfide and Li₂S Redox Conversion in Li-S Batteries. *Small* **2019**, *15*, 1906132.
- (48) Fu, Y.; Wu, Z.; Yuan, Y.; Chen, P.; Yu, L.; Yuan, L.; Han, Q.; Lan, Y.; Bai, W.; Kan, E.; Huang, C.; Ouyang, X.; Wang, X.; Zhu, J.; Lu, J. Switchable encapsulation of polysulfides in the transition between sulfur and lithium sulfide. *Nat. Commun.* **2020**, *11*, 845.
- (49) Huang, S.; Lim, Y. V.; Zhang, X.; Wang, Y.; Zheng, Y.; Kong, D.; Ding, M.; Yang, S. A.; Yang, H. Y. Regulating the polysulfide redox conversion by iron phosphide nanocrystals for high-rate and ultrastable lithium-sulfur battery. *Nano Energy* **2018**, *51*, 340–348.
- (50) Li, Y.; Zhou, P.; Li, H.; Gao, T.; Zhou, L.; Zhang, Y.; Xiao, N.; Xia, Z.; Wang, L.; Zhang, Q.; Gu, L.; Guo, S. A Freestanding Flexible Single Atom Cobalt Based Multifunctional Interlayer toward Reversible and Durable Lithium Sulfur Batteries. *Small Methods* **2020**, *4*, 1900701.
- (51) Yuan, H.; Chen, X.; Zhou, G.; Zhang, W.; Luo, J.; Huang, H.; Gan, Y.; Liang, C.; Xia, Y.; Zhang, J.; Wang, J.; Tao, X. Efficient Activation of Li₂S by Transition Metal Phosphides Nanoparticles for Highly Stable Lithium—Sulfur Batteries. *ACS Energy Lett.* **2017**, *2*, 1711–1719.

